This is a reduced size version of the supp material. The higher res version can be obtained from the AGU webpage for the paper.

Supporting Information for
"Role of (sub)mesoscale generated vertical velocities in tracer subduction"

Dhruv Balwada[1], **Shafer Smith**[1], **and Ryan Abernathey**[2]

[1]Courant Institute of Mathematical Sciences, New York University, New York, New York, USA

[2]Lamont-Doherty Earth Observatory, Columbia University, Palisades, New York, USA

Contents

Additional Supporting Information (Files uploaded separately)

1. Movies showing the tracer uptake at different resolutions

Model Setup

A series of numerical experiments was carried out using the MITgcm ocean model [*Marshall et al.*, 1997a,b]. The hydrostatic Boussineq primitive equations are solved on a Cartesian grid and using a β-plane approximation. The domain is centered at 35S, so that the deformation radius is somewhat larger than in the Southern Ocean, allowing a wider range of sub-deformation scales to be resolved. No-slip and no-flux boundary conditions were imposed at the side walls and the bottom. Exact numerical parameters used are presented in Table 1.

Overview of the Solution

In this section we describe and present some features of the model solution that were not completely necessary to present in the main document.

Corresponding author: Dhruv Balwada, `db194@nyu.edu`

Table 1. Model Parameters and Forcing

Parameter	Value
Horizontal Resolution	20 km, 5 km, 1 km
Vertical Resolution	76 levels (1 m near surface, 150 m near bottom, same as LLC4320)
Time Step	1200 s, 300 s, 40 s
Spin up	20 km: 200 years
	5 km: 100 years (starting from 20 km)
	1 km: 5 years (starting from 5 km).
f_0, β	$-0.83 \times 10^{-4}\text{s}^{-1}$, $1.87 \times 10^{-11}(\text{ms})^{-1}$ (corresponding to 35^oS)
Topography	$-H + h_0 e^{-x^2/\sigma^2}$
	(h_0 = 1000m, σ = 75km)
Wind Stress	$0.2 \sin^2(\frac{(y-100/2)\pi}{2000-100})$ N/m^2
	(with 50 km buffer zones on north and south boundary with 0 N/m^2.)
Temperature restoration	$8(y/2000)\ ^o$ C
Temp restoration piston velocity	1/3 m/day $\sim 3.86 \times 10^{-6}$ m/s
Tracer restoration	1 at top grid point (assigned arbitrary units of kg/m^3)
Tracer restoration piston velocity	$1/72$m/min $\sim 2.3 \times 10^{-4}$ m/s
Bottom quadratic drag	0.0021
EOS Linear with α	2×10^{-4} K^{-1}
viscC4Leith	2.15
viscC4Leithd	2.15
viscAr	5.6614×10^{-4}
viscA4GridMax	0.8
Temp and tracer advection scheme	7th order one-step method w/monotonicity preserving limiter

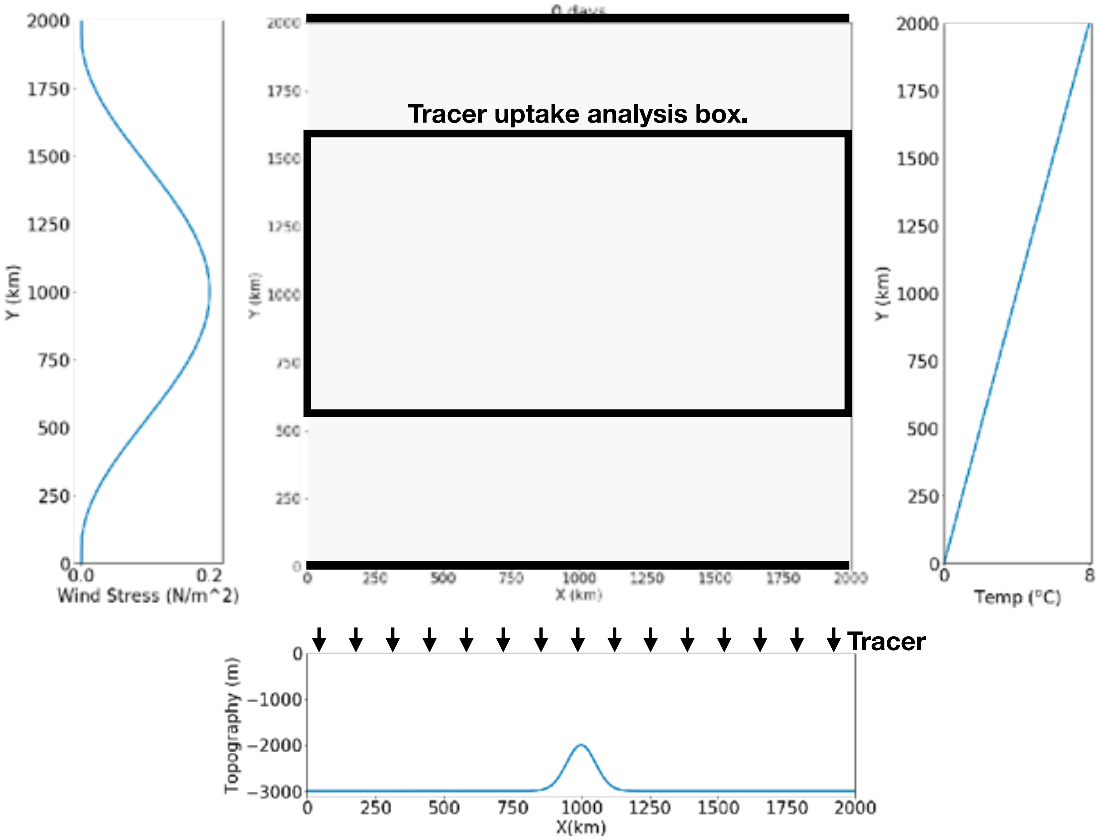

Figure 1. A sketch of the experimental setup. Top left shows the forcing wind stress profile. Top center shows the domain, with bold north and south lines representing walls, and box in the center representing the region over which the tracer budget analysis was performed. The model was zonally periodic. Top right shows the surface temperature restoration profile. Bottom panels shows a zonal profile of the bottom topography, the topography profile does not vary in the meridional direction.

An eastward ocean current arises in response to the forcing, which is composed of a few mean jet like features (Figure 2), and large scale meander originating over the ridge and extending in the downstream direction. The isopycnals rise towards the surface in the south, and are strongly perturbed in the zonal direction by the presence of the ridge (Figure 3). The mean buoyancy frequency shows the presence of a thermocline rising from approximately 1000m in the north to the surface in the south. There is also some indication of a mode water like low stratification layer present above the thermocline, which broadly originates at the surface in regions of Ekman downwelling (Figure 4). The deep ocean has very low, unrealistically low, stratification.

The no-flux boundary condition in combination with no explicit interior mixing, implies that the interior is primarily adiabatic (to the accuracy of the numerics) and that there is no deep meridional overturning circulation [*Marshall and Radko*, 2006]. A shallow overturning circulation that extends to the base of the diabatic layer does form (not shown), which provides a return pathway for the northward Ekman transport near the surface. The surface temperature restoration results in a time mean surface heat flux (Figure 5), which is largely insensitive to the model resolution. In a steady state the net area integrated heat flux is zero, as no water mass leaves the domain.

Maps of vertical velocity near the surface (Figure 6) clearly shows the presence of numerous fronts, which strengthen and increase in number as the resolution is increased. The vertical velocity at depth (Figure 7) shows vertical velocities that are associated with strong mesoscale eddies and enhanced in the downstream region. The fronts near the surface are also stronger in the downstream region, but the contrast in strength of the associated vertical velocities relative to the upstream region decreases as the resolution is increased. The vertical velocities in the 1km simulation are riddled with small scale inertia-gravity waves.

PDFs of surface vorticity (Figure 8) show that the surface vorticity can be almost an order of magnitude higher than the planetary vorticity in the higher resolution simulations, indicating the presence of strong ageostrophic flows. These PDFs also show the canonical skewed distribution that is commonly seen in surface vorticity maps from other high resolution simulations [*Capet et al.*, 2008].

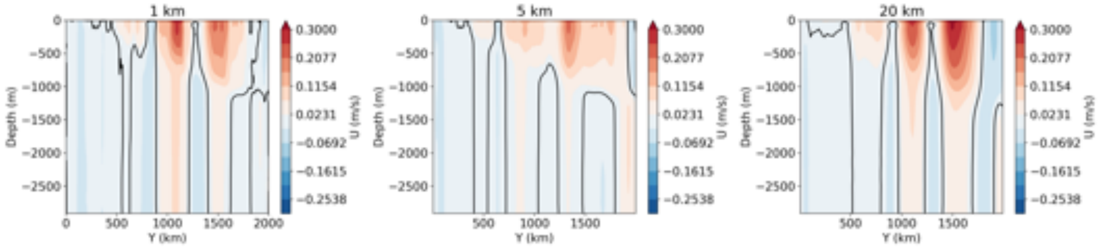

Figure 2. A depth vs. meridional section of the annual mean zonal velocity section at $x = 1000$ km for different resolutions, where the average is taken during the year of the tracer experiment.

Tracer Solution

Figure 9 shows the evolution of the mean tracer and horizontal tracer variance as a function of depth. As discussed in the main text, the tracer concentrations are relatively homogeneous in the well mixed mixing layers and decay rapidly below that. The strongest vertical concentration gradients are at the base of the mixed layer, and are strongest in the lowest resolutions. This is because the lower resolutions simulations is relatively inefficient at transporting tracer through the base of the mixing layer. The tracer variance, presumably in correspondence to the vertical tracer gradient, is the highest near the base of the mixing layer. Except in the 1km simulation at later time, when the strongest tracer variance has migrated to depth.

Figure 10 shows accumulation as a function of depth relative to the accumulation in the 20km simulation. The higher resolution simulations have more tracer accumulation at depth. It is interesting to note that the 5km simulation seems to have slightly more tracer than the 1km simulation below depth of 600m. However, there was very small amount of tracer that penetrated below this depth in the 1 year of the tracer experiment, and the greater accumulation in the 5km simulation could simply have resulted from few isolated tracer penetration event.

Details of Spectral Analysis

Here we present an overview of the calculation of power spectra and cross spectra, and refer the reader to *Uchida et al.* [2017]; *Abernathey and Wortham* [2015] for details on the discrete implementation that is required for numerical models.

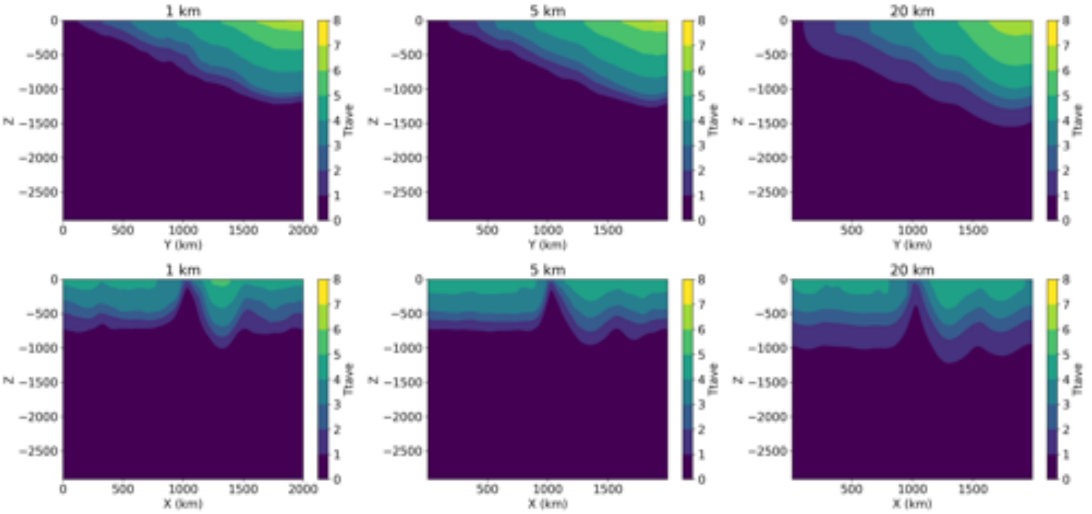

Figure 3. Depth vs. meridional (top) and depth vs zonal (bottom) sections of mean temperature (same as isopycnals), averaged over the year of the tracer experiment.

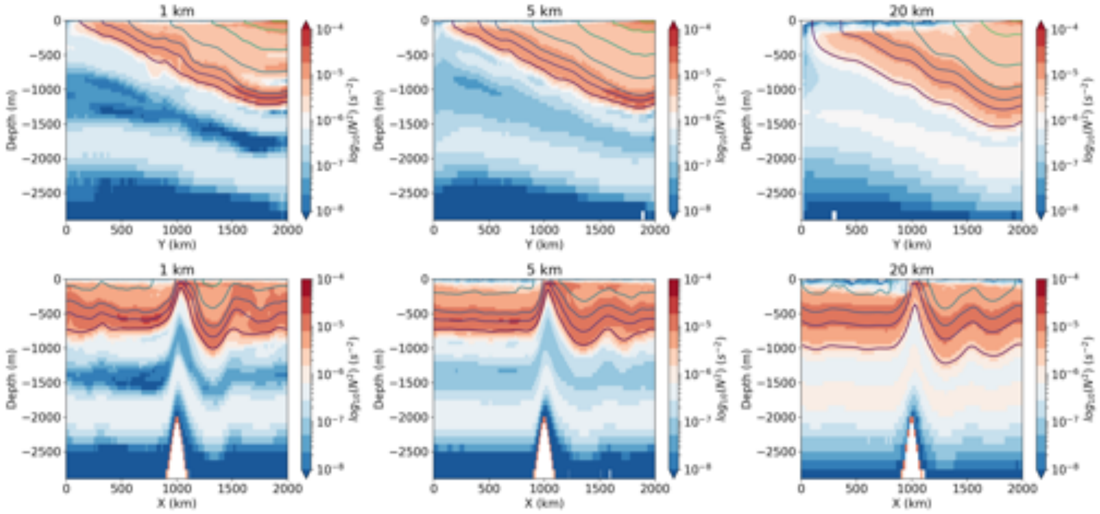

Figure 4. Depth vs. meridional (top) and depth vs zonal (bottom) sections of mean buoyancy frequency, averaged over the year of the tracer experiment. The colored contour lines represent the mean temperatures.

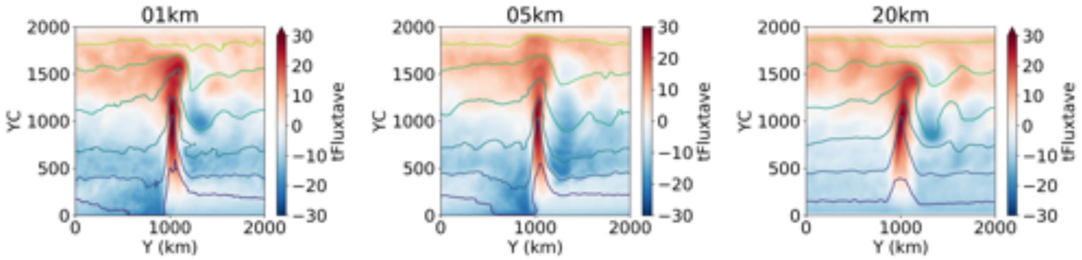

Figure 5. Mean surface fluxes of heat (W/m^2) as a function of resolution, positive heat fluxes imply heating of surface water. Colored contour lines are the mean sea surface temperature.

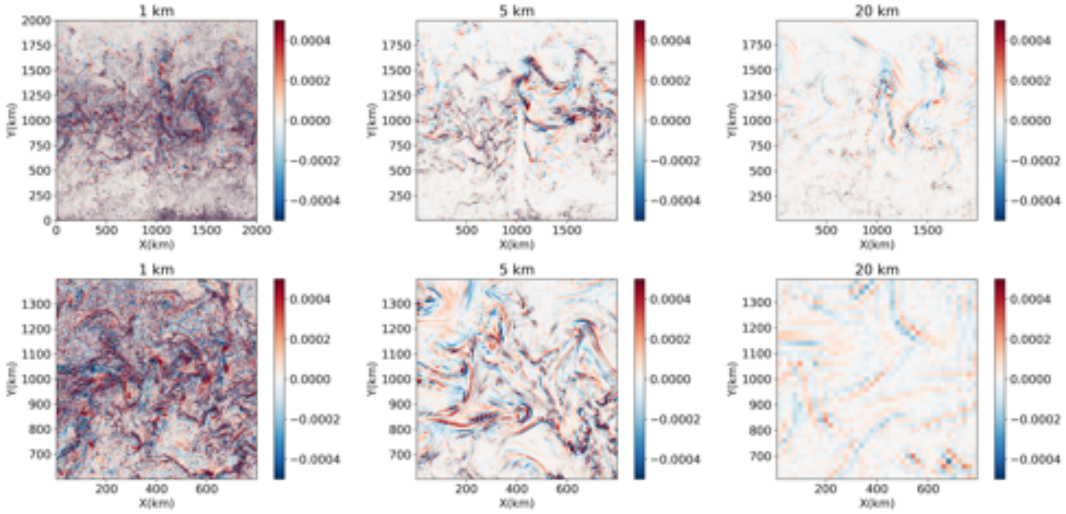

Figure 6. Vertical velocity at a depth of 100 m below the surface at different resolutions in the entire domain (top) and the upstream region (bottom).

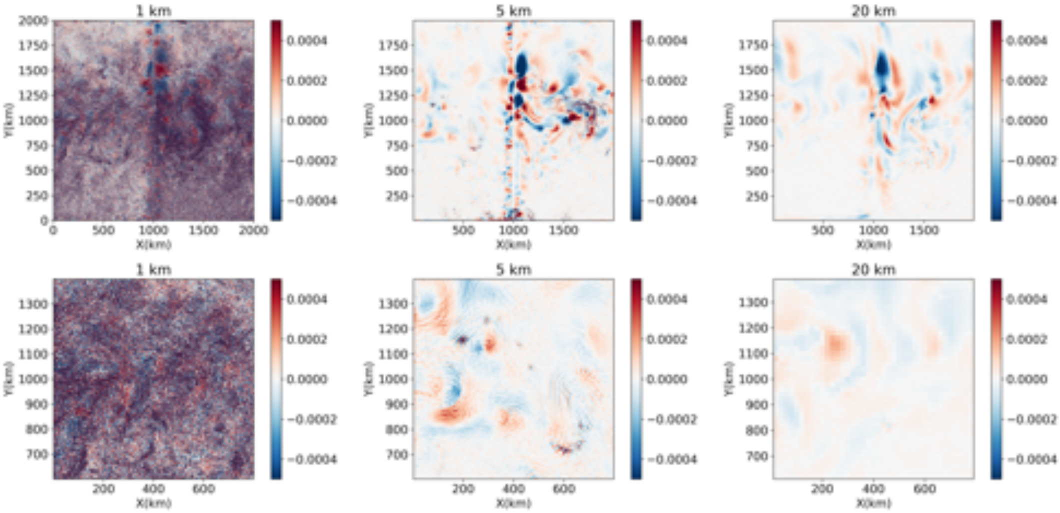

Figure 7. Vertical velocity at a depth of 1500 m below the surface at different resolutions in the entire domain (top) and the upstream region (bottom).

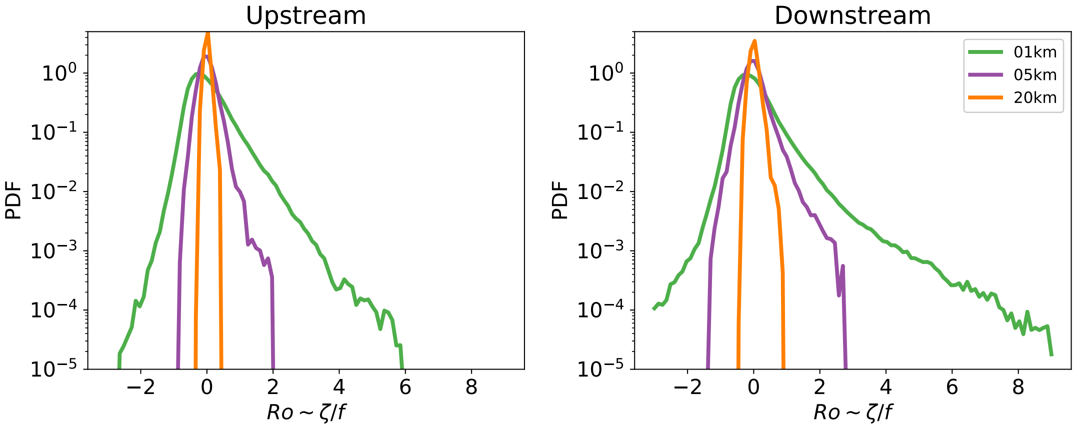

Figure 8. Surface vorticity PDFs for the upstream and downstream regions at different resolutions.

The Fourier transform of any arbitrary quantity along the horizontal space and time axis is defined as

$$A(x, y, z, t) = \int \int \int \hat{A}(k, l, \omega, z) e^{2\pi i(kx + ly - \omega t)}\, dk\, dl\, d\omega. \tag{1}$$

where k and l are the horizontal wavenumbers, and ω is the frequency. The dependency on z is left untouched, as we do not transform along that axis. Using the Parseval's theorem, the mean vertical tracer flux can be written as

$$\overline{wC}(z) = \frac{1}{TL_xL_y} \int_0^T \int_{L_x} \int_{L_y} w(x, y, z, t) C(x, y, z, T)\, dx\, dy\, dt = \int_0^\infty \int_0^\infty \mathcal{R}\{\hat{w}^* \hat{C}\}(k_r, \omega, z)\, dk_r\, d\omega, \tag{2}$$

where $k_r = \sqrt{k^2 + l^2}$ is the isotropic wavenumber. The integrand on the RHS, $\mathcal{R}\{\hat{w}^* \hat{C}\}$, is referred to as the cross-spectra, and portrays the contribution to the vertical tracer flux in wavenumber-frequency space.

Similarly, the power spectrum of vertical velocity, or any other variable, in wavenumber frequency space can also be calculated to provide a decomposition of the energy,

$$\overline{w^2}(z) = \frac{1}{TL_xL_y} \int_0^T \int_{L_x} \int_{L_y} w(x, y, z, t)^2\, dx\, dy\, dt = \int_0^\infty \int_0^\infty \mathcal{R}(\hat{w}^* \hat{w})(k_r, \omega, z)\, dk_r\, d\omega. \tag{3}$$

It should be **noted** that the power spectrum and cross spectrum are defined for mean quantities, rather than sums that were used in the tracer budgets.

As all the results of the spectral analysis are plotted on log axis, instead of plotting the spectrum we usually plot the **variance preserving power spectrum**. This is obtained by observing the following relationship

$$\int_0^\infty E(k) dk = \int_0^\infty kE(k)\, d\log(k), \tag{4}$$

where $E(k)$ is any arbitrary spectrum along an arbitrary axis k. $kE(k)$ is the variance preserving power spectra, and provides the correct visual representation of the relative contributions from different scales on a logarithmic axis.

KPP generated Mixing Layers

The mixing layers in the simulations were generated by the KPP boundary layer parameterization. As the resolution is increased there is more mesoscale eddy activity, leading to more strain induced frontogenesis, and mixed layer baroclinic instability is partially permitted, which together cause the mixed and mixing layer depths to reduce due to the associated restratification. Additionally, the mixing layers show large regional and temporal variability as shown in Figure 11.

The large scale patterns of mixing layer depths (Figure 11b) show three main features — deep mixing layers in the center of the domain, deeper mixing layers on the upstream side of the topography, and very deep mixing layers along the southern boundary. These 3 features can be explained by the large scale forcing and hydrography.

The larger mixing layers in the center (meridional center) are associated with the strongest wind stress forcing, and represent the direct wind generated mixing. The deep mixing layers to the south of the domain are a combined influence of the region having negative heat fluxes (Figure 5) and weak interior stratification producing deep convection like conditions. Shallow mixing layers are present on the downstream side of the topography as a result of stronger eddy activity leading to stronger restratification, and an upstream source of strong stratification located over the topography due to strong heating (Figure 5). The deep mixing layers on the upstream side of the topography are presumably a result of the region being farthest away from the topography, where strong vertical stratification is being generated near the surface by strong heating. Quantifying the relative influence of different mechanisms that produce the observed mixing layer patterns is beyond the scope of this work.

In addition to the large scale patters of mixing layer depths, there is smaller scale temporal and spatial variability that is associated with mesoscale features (Figure 11 a).

Deeper mixing layers have a stronger associated vertical diffusivity, a feature of the KPP parameterization. The produces a region of strong diffusivity on the upstream side of the topographic feature. This deep region of higher diffusivity on the upstream side of the ridge leads to a stronger vertical diffusive flux of tracer on the upstream side of the ridge.

Dispersion Relations, Deformation Radii and Linear Stability Analysis

The MITgcm solves the hydrostatic, Boussinesq, primitive equations. Inertia-gravity waves are a particular set of linear waves that can be supported in this system. The dispersion relationship for inertia-gravity waves in the presence of a constant mean flow, $\mathbf{U_o} = (U_o, V_o)$, is [*Gill*, 1982]

$$\omega_j = \mathbf{k}_h \cdot \mathbf{U}_o \pm f\sqrt{\frac{K_j^2 + |\mathbf{k}_h|^2}{K_j^2}}, \tag{5}$$

where ω is the frequency, $\mathbf{k}_h = (k, l)$ is the horizontal wavenumber, f is the Coriolis frequency, and K_j are the eigenvalues corresponding to the Sturm-Liouville eigenvalue equation for the normal modes, given by

$$\frac{d}{dz}\left(\frac{f^2}{N^2}\frac{d\phi_j}{dz}\right) = -K_j^2\phi_j, \quad \frac{d\phi_j}{dz}(0, -H) = 0, \tag{6}$$

where ϕ_j is the j^{th} vertical mode, K_j is the j^{th} internal deformation wavenumber , $N^2 = db/dz$ is the Brunt-Vaisala frequency, and b is buoyancy. Representative N^2 profiles are plotted in Figure 4.

We numerically integrated the Sturm-Liouville problem using N^2 profile between 200m and the bottom, to calculate the first 6 modes. The top 200m were removed to avoid sharp jumps that might be present in the profile due to the presence of the mixed layer. Figure 13 shows the meridional profile of the the first deformation wavelength in units of km ($L_d = 2\pi/K_1$). We see that L_d varies from approximately 50km to 300km across the meridional extend, and shows little change with resolution. This scale provides a good qualitative estimate of the length scale corresponding to the interior baroclinic instability (discussed below).

The deformation scale corresponding to the mixing layer is approximated as $L_{\text{ML}} = N_{\text{ML}}H_{\text{ML}}/f$. N_{ML} corresponds to the vertical mean of N in the mixing layer, and H_{ML} is the mixing layer depth. This scale provides a good representation of the scale of the fastest growing instability corresponding to the mixed layer instability (discussed below). L_{ML} varies between 0.5 and 2km in all resolution simulations.

We performed a linear stability analysis on the mean state of the solution that was obtained at different resolutions following the method described in *Smith* [2007]. A linear eigenvalue problem (equation 3.2 in *Smith* [2007]) is solved using the mean geostrophic shear and stratification. We used the **oceanmodes** python package (`https://github.com/rabernat/oceanmodes`) to solve the eigenvalue problem. The solution gives frequency (the eigenvalue ω) and normal modes ($\hat{\psi}$) corresponding to each wavenumber. If the frequency has a nonzero positive imaginary part, then the mode is unstable and grows exponentially in time.

The mean stratification and zonal velocity used in the analysis was a temporal mean over a few years and a spatial mean over a 100km by 100km box. The upstream box was centered at ($x = 500$km, $y = 1000$km), and the downstream box was centered at ($x = 1500$km, $y = 1000$km). The structure of the means is different in different regions and the instability properties change accordingly, but the regions chosen over here capture the characteristic properties. Additionally, we set the meridional mean velocity to be zero as it does not qualitatively change the results, except rotating the most unstable wavenumber in the 2D wavenumber plane.

The turbulent, non-wave part of the flow might often follows a power law turbulent dispersion relation of the form [*Vallis*, 2017]

$$\omega \sim [k^3 E(k)]^{1/2}, \tag{7}$$

where $E(k)$ is the energy spectrum for the appropriate variable. In Figure 4a,b of the main manuscript, which are related to the vertical kinetic energy, we show a dashed line representing $\omega \sim k^{3/2}$, which corresponds to a KE spectrum proportional to k^0 — this flat relation is typical of vertical velocity power spectra.

Figure 15 shows that the instability growth rate curves have a peak at wavelength of O(500 m), and associated growth rates of O(1 day). This is the mixed layer instability. The vertical extent of this instability is limited within the mixing layer depth, where the vertical mixing provides the necessary APE to keep the instability active. A second peak at scale at wavelength of O(200 km), and associated growth rates of O(20 days) is present, which is a signature of the interior baroclinic instability. The vertical extent of the amplitude associated with this instability decays rapidly upto depths of the thermocline.

Movies showing structure of vertical tracer transport

The movies show the evolution of the isosurface of tracer concentration 0.1 colored by the surface depth as a function of time, for different resolutions (1,5,20 km). The view is from a northwest corner at depth looking towards the surface and southeastwards.

References

Abernathey, R., and C. Wortham (2015), Phase speed cross spectra of eddy heat fluxes in the eastern pacific, *Journal of Physical Oceanography*, *45*(5), 1285–1301.

Capet, X., J. C. McWilliams, M. J. Molemaker, and A. Shchepetkin (2008), Mesoscale to submesoscale transition in the california current system. part i: Flow structure, eddy flux, and observational tests, *Journal of physical oceanography*, *38*(1), 29–43.

Gill, A. E. (1982), *AtmosphereâĂŤocean dynamics*.

Marshall, J., and T. Radko (2006), A model of the upper branch of the meridional overturning of the southern ocean, *Progress in Oceanography*, *70*(2-4), 331–345.

Marshall, J., A. Adcroft, C. Hill, L. Perelman, and C. Heisey (1997a), A finite-volume, incompressible navier stokes model for studies of the ocean on parallel computers, *Journal of Geophysical Research: Oceans*, *102*(C3), 5753–5766.

Marshall, J., C. Hill, L. Perelman, and A. Adcroft (1997b), Hydrostatic, quasi-hydrostatic, and nonhydrostatic ocean modeling, *Journal of Geophysical Research: Oceans*, *102*(C3), 5733–5752.

Smith, K. S. (2007), The geography of linear baroclinic instability in earth's oceans, *Journal of Marine Research*, *65*(5), 655–683.

Uchida, T., R. Abernathey, and S. Smith (2017), Seasonality of eddy kinetic energy in an eddy permitting global climate model, *Ocean Modelling*, *118*, 41–58.

Vallis, G. K. (2017), *Atmospheric and oceanic fluid dynamics*, Cambridge University Press.

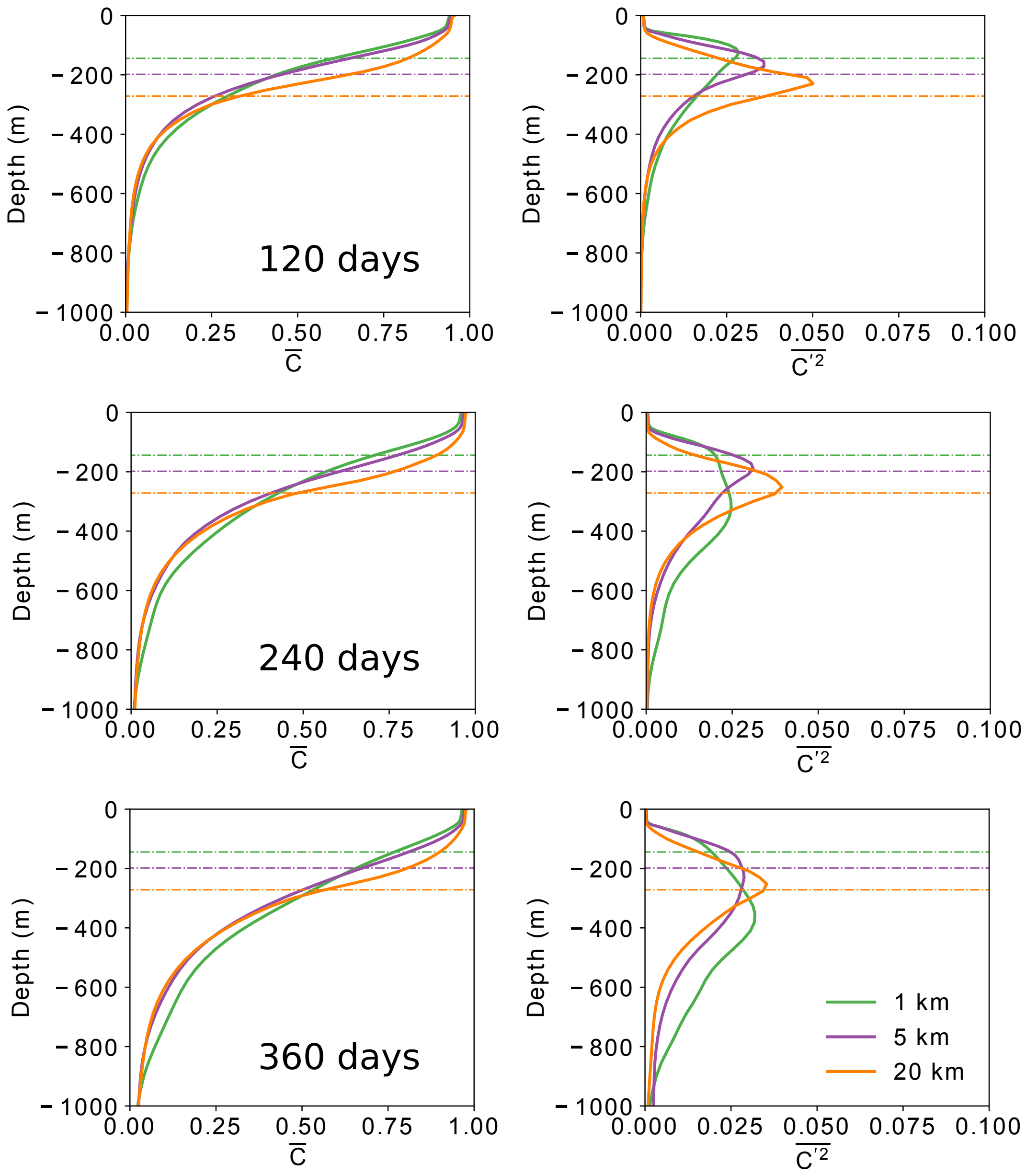

Figure 9. Horizontal mean of tracer concentrations (left) and horizontal variance of tracer concentrations at different times for the different resolutions.

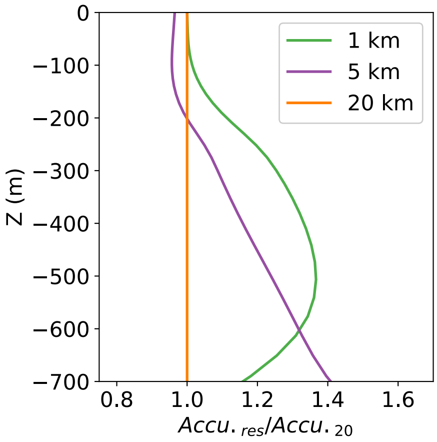

Figure 10. Ratio of accumulation in different simulations to the 20 km simulation.

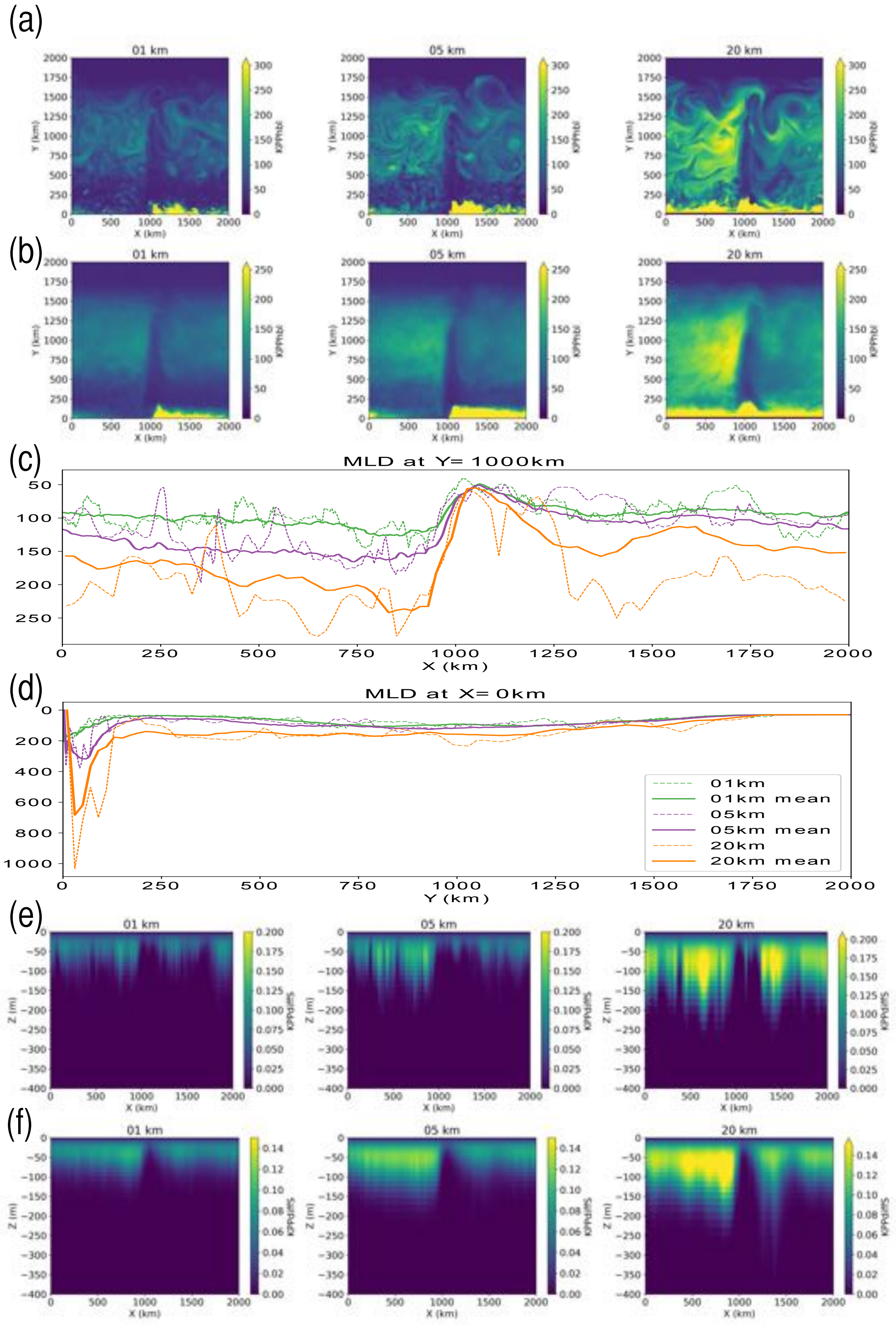

Figure 11. (a) 10 day average maps of mixed layer depth at different resolutions. (b) 1 year average maps of mixed layer depth at different resolutions. (c) Zonal section of mixed layer depth (10 day average — thin dashed, 1 year average — thick solid through the center of the domain (y = 1000km). (d) Meridional section of mixed layer depth (10 day average —thin dashed, 1 year average — thick solid at x = 0km. (e) 10 day average of diffusivity along a zonal section at y = 1000km. (f) 1 year average of diffusivity along a zonal section at y = 1000km.

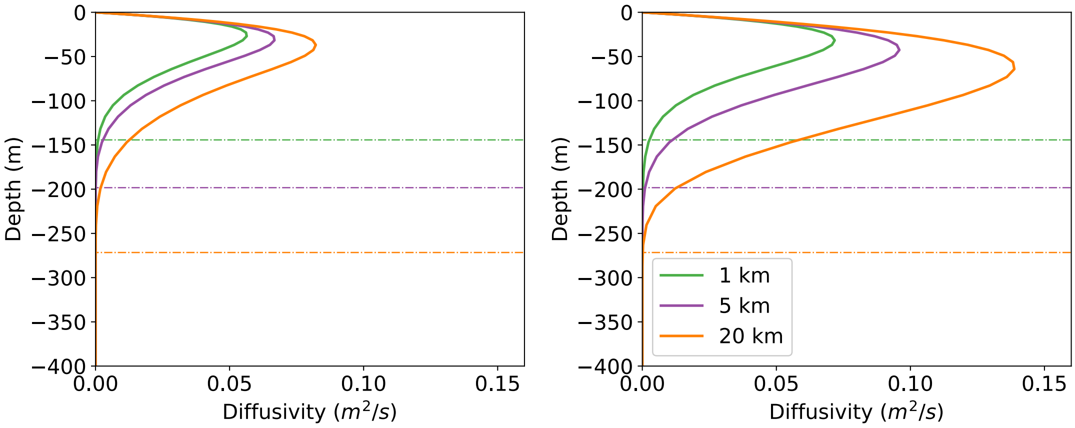

Figure 12. KPP induced diffusivities averaged spatially and at one time snapshot over downstream (left) and upstream (right) regions.

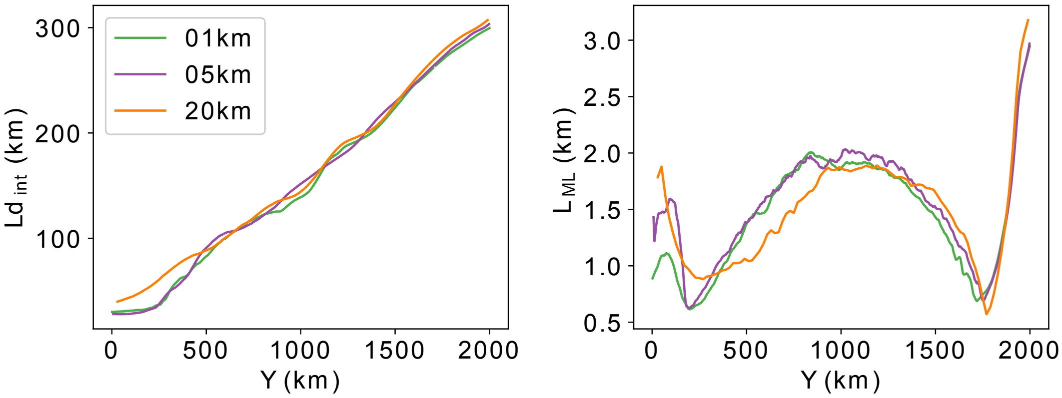

Figure 13. Zonal mean of interior deformation wavelength, $L_d = 2\pi/K_1$ (left), and mixing layer deformation scale , $L_{\mathrm{ML}} = N_{\mathrm{ML}} H_{\mathrm{ML}}/f$ (right) as a function of resolution.

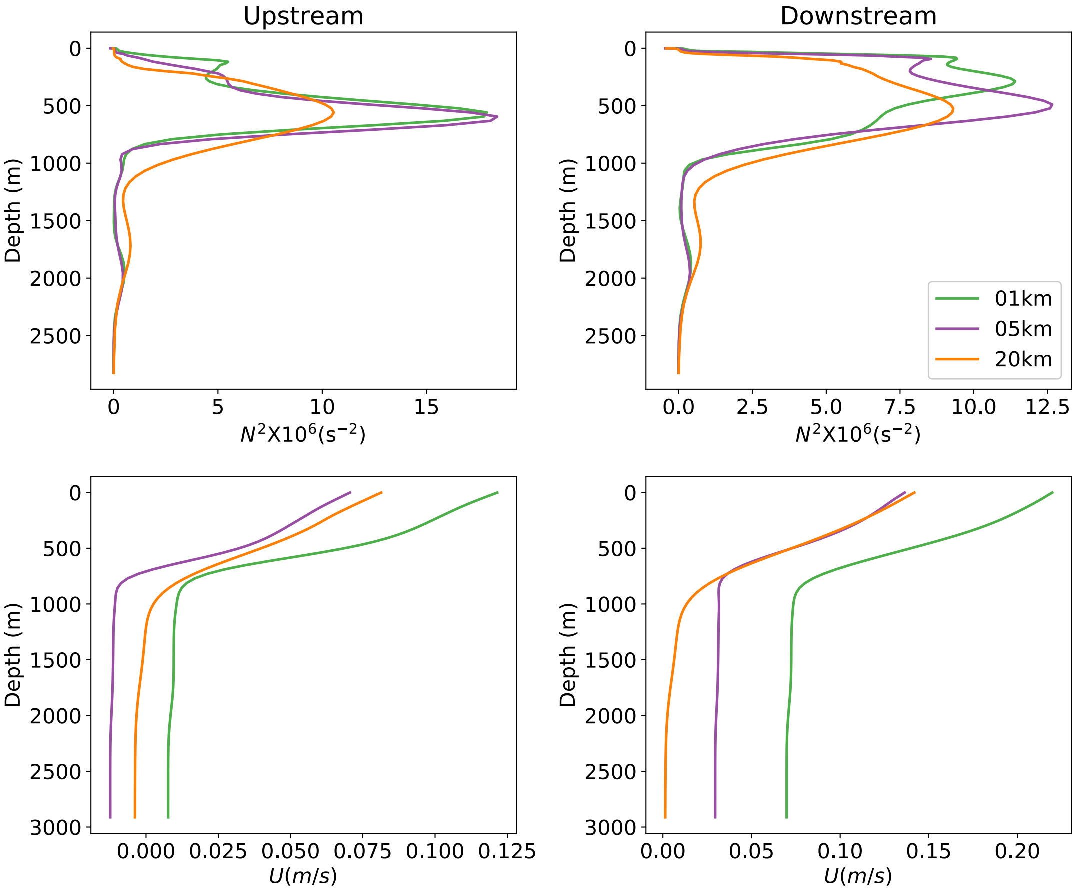

Figure 14. The mean buoyancy frequency (top) and mean zonal velocity (bottom) for the upstream and downstream regions, which was used for the instability analysis.

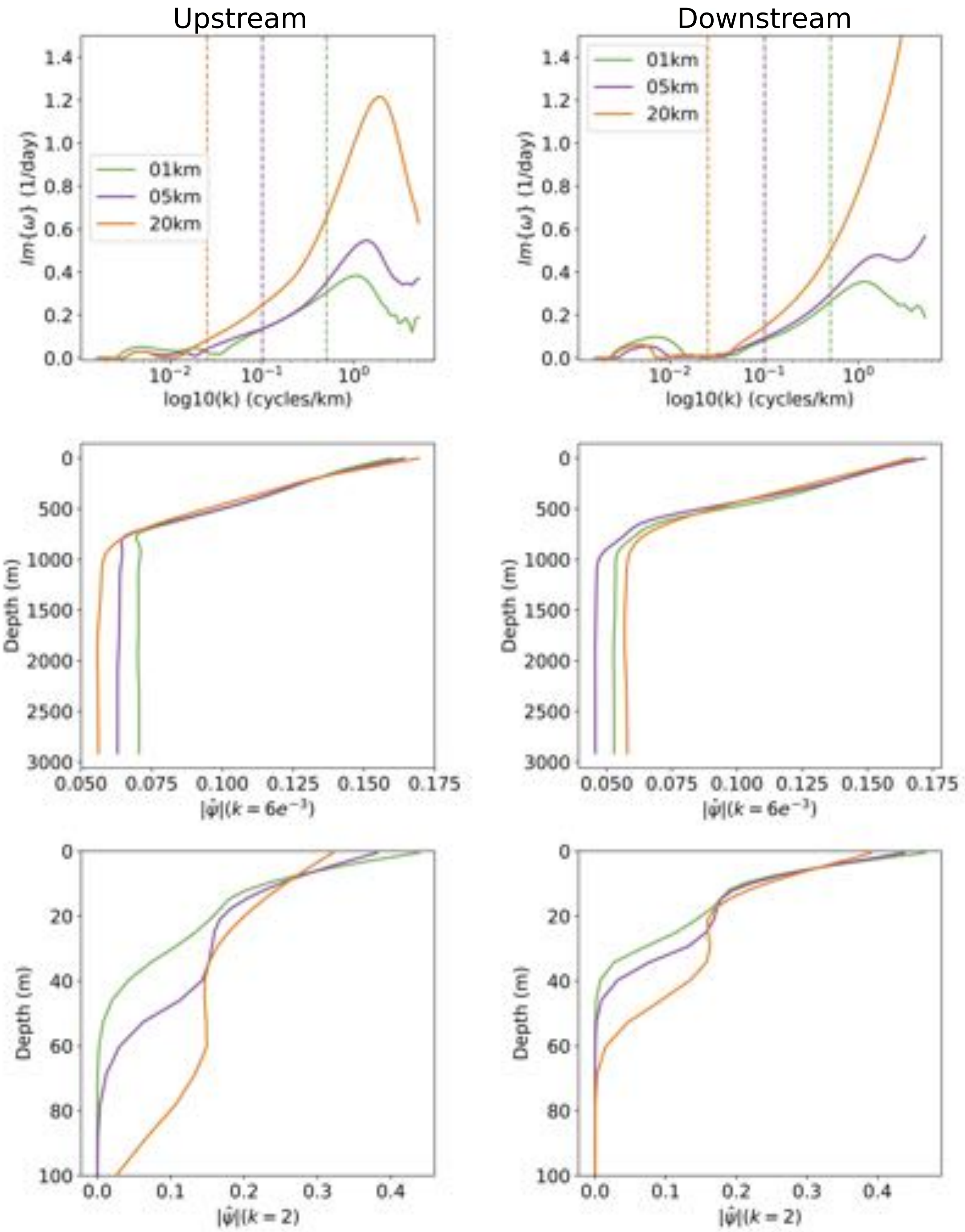

Figure 15. The instability growth rate as a function of zonal wavelength (top) and the vertical structure of the eigenfunction corresponding to interior and mixed layer instability as a function of depth (bottom).